Carbon-Supported IrNi Core−Shell Nanoparticles: Synthesis, Characterization, and Catalytic Activity

Kotaro Sasaki,[†],* Kurian A. Kuttiyiel,[†] Laura Barrio,[†] Dong Su,[‡] Anatoly I. Frenkel,[§] Nebojsa Marinkovic,[⊥] Devinder Mahajan,[∥] and Radoslav R. Adzic[†]

[†]Chemistry Department, [‡]Center for Functional Nanomaterials, and [∥]Department of Energy Science, Brookhaven National Laboratory, Upton, New York 11973, United States
[§]Physics Department, Yeshiva University, 245 Lexington Avenue, New York, New York 10016, United States
[⊥]Department of Chemical Engineering, University of Delaware, Newark, Delaware 19716, United States

S *Supporting Information*

ABSTRACT: We synthesized carbon-supported IrNi core−shell nanoparticles by chemical reduction and subsequent thermal annealing in H_2, and verified the formation of Ir shells on IrNi solid solution alloy cores by various experimental methods. The EXAFS analysis is consistent with the model wherein the IrNi nanoparticles are composed of two-layer Ir shells and IrNi alloy cores. In situ XAS revealed that the Ir shells completely protect Ni atoms in the cores from oxidation or dissolution in an acid electrolyte under elevated potentials. The formation of Ir shell during annealing due to thermal segregation is monitored by time-resolved synchrotron XRD measurements, coupled with Rietveld refinement analyses. The H_2 oxidation activity of the IrNi nanoparticles was found to be higher than that of a commercial Pt/C catalyst. This is predominantly due to Ni-core-induced Ir shell contraction that makes the surface less reactive for IrOH formation, and the resulting more metallic Ir surface becomes more active for H_2 oxidation. This new class of core−shell nanoparticles appears promising for application as hydrogen anode fuel cell electrocatalysts.
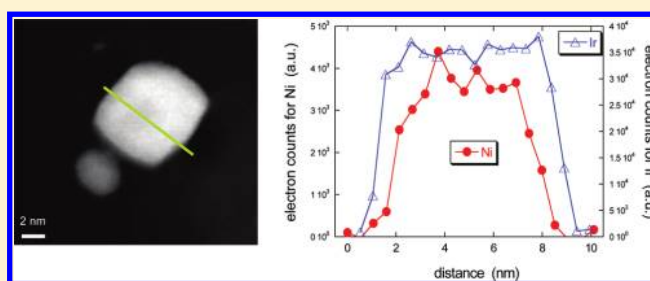
1. INTRODUCTION

In responding to the needs of modern society and emerging ecological concerns, it is now essential to develop new, inexpensive, and environmentally friendly energy conversion and storage systems. The performance of these devices depends fundamentally on the properties of their materials. Nanostructured core−shell materials are becoming increasingly attractive for these purposes because they often exhibit better physical and chemical properties than their single-component counterparts and alloys; hence, they are potentially useful over a broader range of applications. During the past decade, immense efforts have been made to fabricate core−shell materials with tailored structural, optical, and catalytic surface properties.[1−12]

The choice of metals for the shell and core of bimetallic nanoparticles is based on the segregation properties of the two metals,[13,14] as well as their electronic and strain-inducing effects.[16,17] The chemical composition at the surface of an alloy may differ from that in the bulk; that is, one of the components of the alloy may be enriched in the surface region. At elevated temperatures, the atoms of some noble metals tend to segregate to the surface;[6,18−21] the formation of a complete noble metal shell can protect the non-noble-metal core from oxidation or dissolution. Therefore, the durability of the core−shell nanoparticles depends greatly on the integrity of the shell's structure.

Detailed characterization of the atomic structure of nanoparticles is a prerequisite for understanding the origins of their properties such as activity and durability. It has been known that the combination of the scanning transmission electron microscope (STEM) and electron energy-loss spectroscopy (EELS) can provide detailed information on the structures of individual nanoparticles, while X-ray absorption spectroscopy (XAS) and X-ray diffraction (XRD) offer average information on atomic structures from thousands of nanoparticles.[22,23] These techniques are thus complementary, and by combining their results at the stages of data analysis and modeling, we can fully characterize core−shell nanoparticles.

In this communication, we present a simple method of synthesizing carbon-supported IrNi core−shell nanoparticles comprising IrNi alloy cores completely covered with Ir shells. The procedure is very facile and applicable to large-scale synthesis. The core−shell structure was characterized by XRD, STEM−EELS, and in situ XAS. To investigate the effect of annealing temperature on its formation of core−shell structure, we employed time-resolved synchrotron XRD studies together

with Rietveld refinement analyses. This new class of core—shell nanoparticle catalyst showed the higher mass activity of H_2 oxidation in an acidic solution than that of a commercial Pt/C catalyst.

2. EXPERIMENTAL DETAILS

2.1. Synthesis. The carbon-supported iridium and nickel core—shell nanoparticles were prepared as follows. An equal molecular ratio of $(NH_4)_2IrCl_6$ and $Ni(HCO_2)\cdot 2H_2O$ salts was mixed with high-area Vulcan XC72R carbon black to obtain a loading of 20 wt % total metal. The mixture was dissolved in Millipore water and purged with Ar in an ultrasonic bath for an hour. The salts were then reduced by adding $NaBH_4$ while simultaneously purging the mixture with Ar. The mixture obtained was washed and rinsed with Millipore water and then dried. The sample was annealed at 600 °C under 15% H_2/Ar gas for 2 h in a tube furnace. The H_2 environment was necessary to completely reduce both Ni and Ir (Supporting Information, Figure S5) and the annealing temperature (600 °C) was chosen to securely induce the core—shell structure. Chemical analysis of the resultant IrNi sample was carried out using energy-dispersive X-ray (EDX) equipped with a JEOL JEM2100F transmission electron microscope. The mean mole ratio of Ni to Ir (x_{Ni}/x_{Ir}) determined from eight particles was 0.56 with a standard deviation of 0.04. It should be emphasized that this low standard deviation denotes that the compositions of the particles are virtually identical.

2.2. X-ray Diffraction. XRD measurements were taken with a Phillips 3100 diffractometer using Cu Kα radiation (1.54056 Å). Samples for analysis were obtained by loading the slurries onto a glass slide, followed by drying them in air. The diffraction patterns were collected from 20° to 80° at a scanning rate of $0.6° \text{ min}^{-1}$, with a step size of 0.02°.

2.3. STEM—EELS. The Hitachi aberration-corrected scanning transmission electron microscope (HD-2700C) at the Center for Functional Nanomaterials (CFN), Brookhaven National Laboratory (BNL) was used. For this study, we used a 1.4 Å electron probe with probe current ~50 pA. The microscope is equipped with a cold field emission electron source with energy resolution of 0.35 eV. The carbon-supported nanoparticles were dispersed in water, and one drop of the slurry was deposited on a carbon-covered copper grid (EMS, Hatfield, PA).

2.4. In Situ XAS Studies. Two kinds of in situ XAS measurements were undertaken at the National Synchrotron Light Source (NSLS), BNL at the X19A and X18B beamlines. One was in situ electrochemical XAS experiments; the XAS cell was incorporated into a three-electrode configuration. The IrNi sample (working electrode), a proton exchange membrane (Nafion 117, DuPont Chemical Co., DE), and a Pt thin foil (counter electrode) were sandwiched and clamped tightly by the two acrylic plastic bodies. Each plastic body has an X-ray window. The electrolyte was 1 M $HClO_4$, and an Ag/AgCl leak-free electrode was used as a reference electrode. All potentials in this contribution are quoted with respect to the reversible hydrogen electrode (RHE). The measurements were carried out at the Ir L_3 edge (11215 eV) and Ni K edge (8333 eV) at different potentials at room temperature. This electrochemical cell was designed for acquiring XAS data in both the transmission and fluorescence modes, although the data presented below were obtained in the former. Details of the electrochemical cell, which is a modified version of that described in ref 40, are given elsewhere.[41] The other kind of experiments consisted of in situ

thermal XAS measurements; the experimental cell we used is pictured elsewhere.[42] Approximately 100 mg of carbon-supported IrNi particles, which were reduced only by $NaBH_4$ but were not annealed in H_2 atmosphere, were compressed into a circular disk at room temperature; the disk was installed on a holder with a window, through which X-rays impinged on the sample disk. A resistance heater, embedded inside the holder, annealed the sample at given temperatures up to 400 °C. We monitored the annealing temperature with a thin chromel—alumel thermocouple placed near the sample. The thermal reactor cell was shielded with a thin Kapton film, in which a gas containing 5% H_2 in He was flowed (10 mL/min) during annealing. The measurements were carried out separately at the Ir L_3 edge (11215 eV) and Ni K edge (8333 eV) from room temperature to 400 °C. The data acquired by both the electrochemical and thermal cells were processed and analyzed by Athena and Artemis software.[43]

2.5. In Situ Time-Resolved Synchrotron XRD. The measurements were performed at the X7B beamline at NSLS to detail the formation of core—shell structures during annealing. The instrument parameters (Thompson—Cox—Hastings profile coefficients) were derived from the fit of a LaB_6 reference pattern. Approximately 5 mg of the carbon-supported IrNi nanoparticles, which were reduced only by $NaBH_4$, were loaded in a 1 mm quartz reactor that was attached to a flow system, and annealed up to 600 °C at a heating rate of 4.8 °C/min. A small resistance heater was wrapped around the reactor capillary, and the temperature was monitored with a thin chromel—alumel thermocouple placed inside the capillary near the sample. We maintained a 10 mL/min gas flow containing 5% H_2 in He throughout the annealing process. The wavelength of X-ray used was 0.3184 Å. XRD patterns were recorded on a Mar345 image plate detector during annealing; the recording time for a spectrum is ~2.6 min. Details of the synchrotron XRD experiment were described earlier.[44,45] The Rietveld profile refinements were performed with the aid of GSAS software.[46–48] The series of powder patterns were refined by sequential analysis wherein the starting model is based on the earlier powder pattern.

2.6. Electrochemical Measurement. A thin film of the electrocatalyst was prepared on a glassy carbon rotating electrode (area: 0.164 cm^2) for electrochemical measurements. The electrode was then covered by a small amount of a Nafion solution (5 μL of 4 μg/10 μL) and dried in air before rotating disk electrode measurements. Solutions were prepared from Optima perchloric acid obtained from Fisher and Milli-Q UV-plus water (Millipore). Commercial Pt/C (10 wt %) and Ir/C (10 wt %) from E-TEK were used as received. An Ag/AgCl/KCl (3 M) electrode was used with a double-junction chamber as a reference, and all potentials, E, are quoted with respect to reversible hydrogen electrode (RHE).

3. RESULTS AND DISCUSSION

3.1. Characterization of Core—Shell Structure. Figure 1 shows the XRD pattern measured from the IrNi/C nanoparticles using Cu Kα radiation (1.54056 Å). There are three pronounced reflection peaks at $2\theta = 42.65°$, 49.61°, and 72.42°. No separate peaks for Ir or Ni were observed (the reflection peaks of (111), (200), and (220) planes for Ir and Ni are denoted by the blue and red bars, respectively). The first peak at $2\theta = 42.65°$ is indexed between the Ir (111) and Ni (111) planes at $2\theta = 40.66°$ and 44.51°, respectively. Ir and Ni are known to form a solid solution
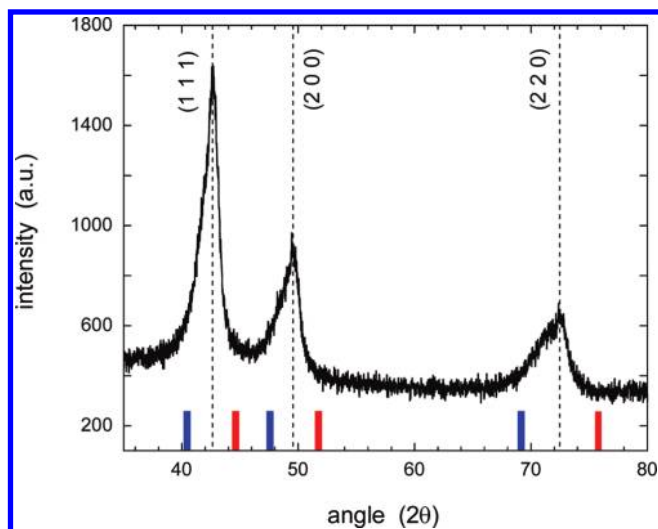
9895

dx.doi.org/10.1021/jp200746j |*J. Phys. Chem. C* 2011, 115, 9894–9902

Figure 1. XRD pattern of carbon-supported IrNi nanoparticles with Cu Kα radiation after annealing at 600 °C in a H_2 atmosphere for 2 h. Blue and red bars designate the $(1\,1\,1)$, $(2\,0\,0)$, $(2\,2\,0)$ reflections from pure Ir and Ni, respectively.

Figure 2. (a) HAADF-STEM image of an IrNi nanoparticle, and (b) comparison of the EELS intensities for the Ir M-edge and Ni L-edge along the scanned line as indicated in (a).

alloy as a bulk at all relative concentrations of the two elements. The phase diagram of Ir–Ni alloy is shown in Supporting Information, Figure S8.[24] The XRD pattern points to the formation of IrNi solid-solution alloy nanoparticles, possibly with a fcc structure ($Fm3m$) with a lattice parameter of $\cong 3.72$ Å. (We note that both Ir and Ni have a fcc structure and that the lattice parameters for Ir and Ni are 3.839 Å and 3.524 Å, respectively.[25]) The average size of the IrNi nanoparticles is 4.7 nm, estimated from Scherer's equation.[26] Another intriguing feature in Figure 1 is that the reflection peaks are asymmetrical, with tails toward the 2θ values of Ir planes. The asymmetry of the XRD peaks may be caused by the Ir shells formed by the segregation of Ir on the surfaces of IrNi solid solution alloy cores during annealing. The concentration change in Ir from the cores to the surfaces appears to be the origin of the tail in the peaks, as discussed below.

STEM–EELS observations were made on some of the nanoparticles. Figure 2a shows a high-angle annular dark field (HAADF) image of a single nanoparticle and 2b compares the EELS intensities from the Ir M-edge and Ni L-edge obtained by moving the electron probe along the line indicated in Figure 2a (we note the arbitrary scales of the y axes). (The EELS spectra for Ni L-edge and Ir M-edge taken at the center of the nanoparticle are shown in Supporting Information, Figure S1.) In Figure 2b, it is evident that the intensities of both Ir and Ni are approximately constant around the center of nanoparticle and that Ir is enriched (or Ni is depleted) at both edges of nanoparticles; the thickness of Ir-enriched layers is ∼0.75−1 nm (3−4 layers). Hence, we clearly demonstrated the formation of the Ir shell. Another STEM−EELS observation on a different IrNi nanoparticle is depicted in Supporting Information, Figure S2. The thickness of Ir-enriched layer is ∼0.25 nm (one layer). By combining the XRD and the STEM−EELS measurements, it is inferred that the core−shell structure consists of Ir-rich top layers on the surfaces of IrNi solid-solution alloy cores.

A low-resolution STEM image and a histogram of the particle size distribution are depicted in Supporting Information, Figure S3. Most particles have round, spherelike shapes, although some are slightly semirounded. Th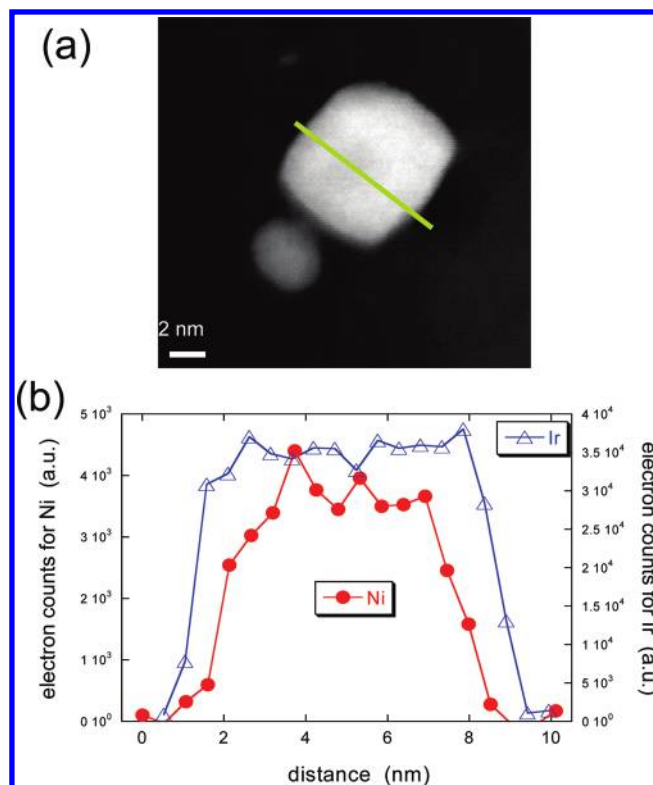e particle size varies from 2 to 10 nm. The average size is 4.8 nm, which is fairly in line with the values determined by the XRD experiments. On the basis of the low-resolution STEM images we approximate the particle shape as a sphere, although the spherelike particles are considered to have various geometries, such as cuboctahedral, polyhedral, and icosahedral structures.[27−29]

Curves a and b of Figure 3 show the in situ X-ray absorption near edge structure (XANES) of the Ir L3 and Ni K edges from the IrNi nanoparticles in 1 M $HClO_4$ at a potential of 0.41 V, together with those from reference materials, viz., Ir black (the particle diameter $\cong 5\,\mu$m) and Ni foil (the thickness $\cong 10\,\mu$m), respectively. The Ni in the IrNi nanoparticles is considered to be metallic because the edge energy (E_0)[30] shows no shift compared with that of the Ni bulk foil (8333 eV). The Ni spectrum from the IrNi nanoparticles also exhibits three peaks at 8348, 8353, and 8378 eV; the energy values are lower, and the peak intensities are higher than those for the peaks from the Ni foil, consistent with the reasonable assumption that alloying with Ir may change the electronic states of Ni atoms, as many XANES studies have reported electronic interaction between alloy components.[4,23,31−33] Also shown in Figure 3b is the Ni K edge spectrum from the IrNi nanoparticles at a potential of 1.11 V. Surprisingly little change is observed between the two spectra at 0.41 and 1.11 V. On the other hand the in situ XANES of Ir L3 edge from the IrNi nanoparticles at 0.41 V displays a decrease in intensity of the white line compared with that from the Ir black (Figure 3a); this suggests that electronic properties of Ir may change by alloying with Ni.

Figure 4 depicts the Fourier transformed extended X-ray absorption fine structure (EXAFS) spectra of the Ir L3 and Ni K edges from the IrNi nanoparticles in 1 M $HClO_4$ at a
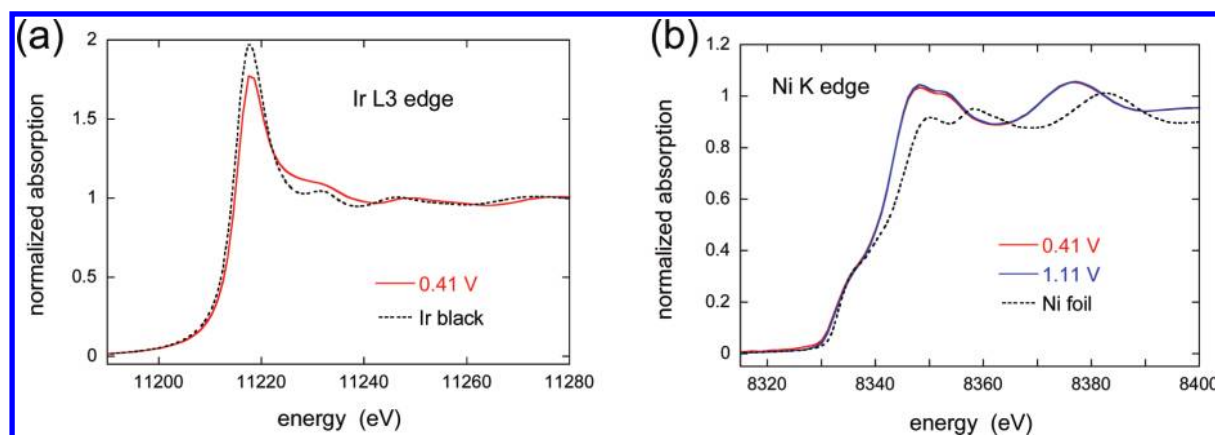
Figure 3. In situ XANES of (a) Ir L3 edge and (b) Ni K edges from the IrNi nanoparticles in 1 M HClO4 at potentials of 0.41 V for (a and b) and 1.11 V for (b). Also shown are spectra from (a) Ir black, and (b) a Ni foil.
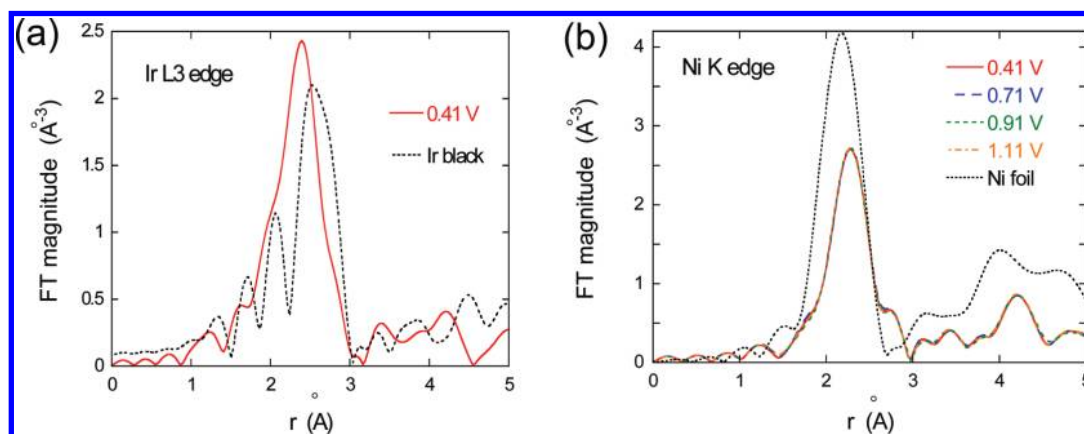

Figure 4. In situ EXAFS Fourier transformed magnitudes of (a) Ir L3 edge and (b) Ni K edge obtained from IrNi nanoparticles in 1 M HClO$_4$ at 0.41 V for (a), and 0.41, 0.71, 0.91, and 1.11 V for (b). Also shown are spectra from (a) Ir black and (b) a Ni foil.

potential of 0.41 V, together with those from their respective reference foils. (The k^2-weighted EXAFS spectra are depicted in Supporting Information, Figure S4.) The differences between the nanoparticles and their reference materials are apparent in the spectra, indicating that the atomic structures surrounding both Ir and Ni in the IrNi nanoparticles are significantly different from those in their 3D bulks. The highest peak in Ni from the IrNi nanoparticles is shifted to a higher r compared with that from the Ni foil, while the highest peak in Ir from the IrNi nanoparticles is displaced to a lower r than that from the Ir black. These figures represent the expansion in the Ni metal (M) bonds and the contraction in the Ir—M bonds as a consequence of the formation of IrNi solid solution alloy cores; the result is in line with those obtained from the XRD measurements (Figure 1) and the EXAFS fitting as discussed below. The EXAFS spectra of Ni K edge from the IrNi nanoparticles at potentials of 0.71, 0.91, 1.11 V also are illustrated in Figure 4b. Little change occurs with increasing potentials, and no characteristic signature of Ni oxides and/or Ni ions (as shown in Supporting Information, Figure S5a) is seen, even at the high potentials. As shown in Pourbaix diagrams,[34] Ni cannot be present in a metallic state when exposed to acid solutions, unless the potential applied is below −0.4 V. The experimental result from the in situ EXAFS indicates that Ni atoms constituting the IrNi cores are not

exposed to the electrolyte since the Ir shell completely encapsulates the IrNi core; Ni in the IrNi solid solution cores therefore is protected from oxidation or corrosion. The voltammetry curve of IrNi nanoparticles (shown in Supporting Information, Figure S7c) also revealed no anodic currents that can be ascribed to the oxidation/dissolution of Ni.

The Ir L3 and Ni K edge data were fitted concurrently with the passive electron reduction factors ($S_0{}^2{}_{Ir}$ and $S_0{}^2{}_{Ni}$) equal to those determined from fitting the Ir black and Ni metal foil data (0.81 and 0.82, respectively). The following constraints were applied: (i) The Ir—Ni bond distance is the same as that measured from either edge (i.e., $R_{Ir-Ni} = R_{Ni-Ir}$); (ii) the bond length disorder parameters of heterogeneous metal bonds are the same as those measured from opposite atoms (i.e., $\sigma^2{}_{Ir-Ni} = \sigma^2{}_{Ni-Ir}$); (iii) the ratio of coordination numbers (N_{Ir-Ni}/N_{Ni-Ir}) reflects the actual molar fractions of the metals (x_{Ni}/x_{Ir}) determined as 0.56 by the EDX analysis; and (iv) the total coordination numbers (N_{Ir-M} and N_{Ni-M}) with a diameter of 4.7 nm are 11, as shown by modeling the core—shell nanoparticle (i.e., $N_{Ir-Ir} = 11 - N_{Ir-Ni}$ and $N_{Ni-Ni} = 11 - N_{Ni-Ir}$). Figure 5 displays the fitting results of the Ir—Ni nanoparticles. Good agreement is given between the fits and the original spectra for both Ir L3 (Figure 5a) and Ni K (Figure 5b) edges. Table 1 summarizes the coordination numbers obtained. (The other structural parameters are listed in Supporting
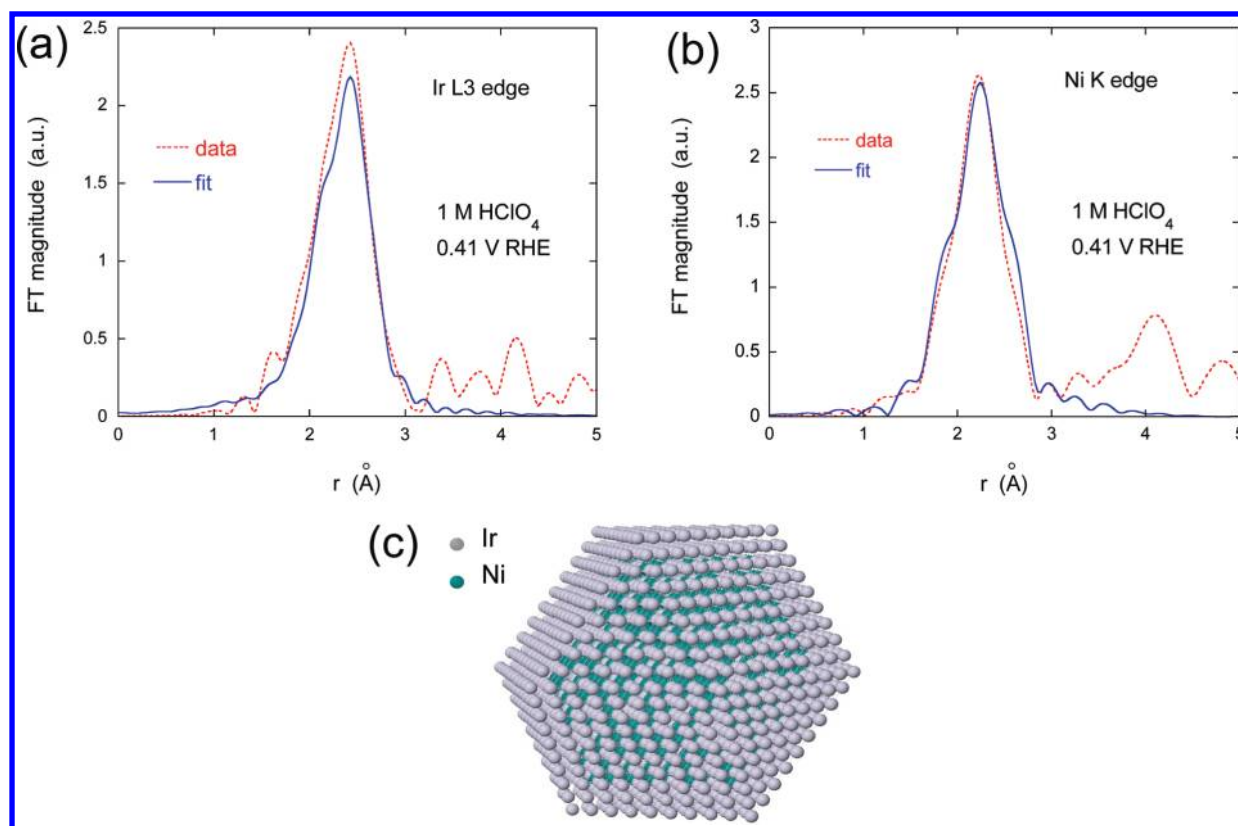
Figure 5. Fourier transform magnitudes of the data (dotted red) and first-shell fit (solid blue) of (a) Ir L3 and (b) Ni K edges from IrNi nanoparticles in 1 M $HClO_4$ at a potential of 0.41 V (c) Atomic configuration of two shell layers of Ir (1454 atoms) on an IrNi alloy core (1030 Ni and 385 Ir atoms). Ir: gray spheres. Ni: green spheres. Atomic ratio of Ni/Ir: 0.56. Diameter: 4.68 nm. Average metal—metal coordination number: 11.

Table 1. Coordination Numbers Determined by the EXAFS Experiment, and One-Layer Ir Shell and Two-Layer Ir Shell Models

	N_{Ir-Ir}	N_{Ir-Ni}	N_{Ni-Ni}	N_{Ni-Ir}	N_{Ir-Ni}/N_{Ni-Ir}	N_{Ni-Ni}/N_{Ni-Ir}
EXAFS	8.1 ± 0.7	2.9 ± 0.7	5.9 ± 0.7	5.1 ± 0.7	0.56	1.2 ± 0.2
one-layer Ir shell	6.47	3.76	5.28	6.72	0.56	0.79
two-layer Ir shell	7.82	2.42	7.69	4.31	0.56	1.78

Information, Table S1.) We note that the length of the Ir—Ir bond obtained (2.664 Å) is less than that of pure Ir (2.714 Å), while the Ni—Ni bond obtained (2.562 Å) obtained is longer than that of pure Ni (2.492 Å), indicating their alloying, vide supra.

The interpretation of the coordination numbers obtained is not straightforward since they are the ensemble-average values from both the shells and cores, except for N_{Ni-Ni} that is derived only from the cores. For an A—B binary solid-solution random alloy, the ratio (relative to the A atom) of the coordination number N_{A-A} to N_{A-B} is equal to the mole fraction ratio x_A/x_B of the elements in the bulk,[24] i.e., $N_{A-A}/N_{A-B} = x_A/x_B$. As listed in Table 1, the ratio of coordination numbers N_{Ni-Ni}/N_{Ni-Ir} is 1.2, which is much larger than the actual mole fraction ratio $x_{Ni}/x_{Ir} = 0.56$. This finding indicates that more Ni—Ni bonds (and fewer Ni—Ir bonds) are present than in a random alloy wherein the two atoms have statistical distribution; this finding is well consistent with the STEM observations showing the Ir-rich (or Ni-depleted) shells; in the cores the number of Ni—Ni bonds should be larger than on the average.

We used a suite of programs that model polyhedral nanoparticles with different diameters, different Ir shell thicknesses, and different molar ratios of IrNi cores to calculate the atomic coordination numbers for various core—shell structures.[36,37] We then compared the coordination numbers in the model with those from the EXAFS analysis in order to determine the most suitable core—shell structure. We employed the polyhedron model to approximate a sphere-shaped particle for the present system. Table 1 also lists the calculated coordination numbers from two core—shell models: one comprises a one-layer Ir shell (812 atoms) on an IrNi alloy core (1027 Ni and 1030 Ir atoms), while the other represents a two-layer Ir shell (1454 atoms) on an IrNi alloy core (1030 Ni and 385 Ir atoms). Ir and Ni atoms in the cores are randomly alloyed via a random number generator. For both models, the atomic ratio of Ni/Ir was set at 0.56, the diameter was calculated as 4.68 nm, and the average (metal—metal) coordination numbers were estimated to be 11. The two-layer model fits most of the EXAFS data much better cumulatively than does the one-layer model. Thus, the EXAFS analysis is consistent with the model wherein the IrNi nanoparticles are composed of two-layer Ir shells and IrNi alloy cores, as Figure 5c schematically shows. On the basis of this result together with those from the XRD and the STEM—EELS measurements, we conclude that the nanoparticles comprise core—shell structure with Ir-rich top layers on the surfaces of IrNi solid-solution alloy cores.
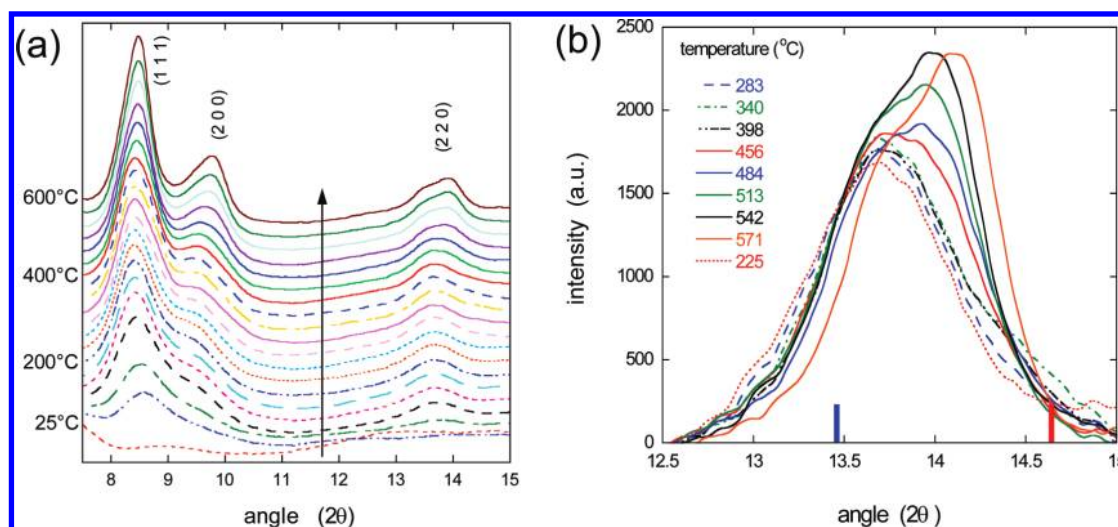
Figure 6. (a) In situ time-resolved XRD patterns (the wavelength: 0.3184 Å) obtained from the IrNi nanoparticles (reduced only by NaBH$_4$ before the test) during reduction in 5% H$_2$/He flow at increasing temperatures (a heating rate of 4.8 °C/min). (b) Details of in situ time-resolved XRD patterns obtained from the IrNi nanoparticles between (2θ =) 12.5° and 15° at annealing temperatures from 225 to 571 °C. Blue and red bars designate a (2 2 0) reflection from pure Ir and Ni, respectively.

3.2. Formation of Ir Shells on IrNi Cores During Thermal Treatment. To understand the effect of thermal treatment in a H$_2$ environment on the formation of core−shell structure in IrNi nanoparticles, time-resolved XRD measurements were carried out. (In situ thermal XAS measurements were also performed. The results are described in Supporting Information, Figure S5.) Figure 6a depicts the in situ time-resolved XRD patterns collected during the annealing process (the wavelength: 0.3184 Å); the IrNi/C sample reduced only by NaBH$_4$, was loaded into a quartz reactor and annealed from room temperature up to 600 °C with a flow of 5% H$_2$/He gas mixture. No prominent diffraction peaks were observed at room temperature (dashed red curve), indicating that the initial sample had no long-range ordered structure; rather, it has partially reduced Ir and Ni, as shown in Supporting Information, Figure S5, which must form small clusters with short-range atomic order. However, as temperature increases (designated by the arrow in the figure), three diffraction features appear, and the peaks become more intense as the temperature rises.

Figure 6b illustrates details of the in situ XRD patterns between (2θ =) 12.5° and 15° at annealing temperatures from 225 to 571 °C.[27] As demonstrated in Supporting Information, Figure S5, both Ir and Ni in the IrNi sample must have been fully reduced up to 220 °C. Although the observed peaks lie between the reflections from Ir(2 2 0) (2θ = 13.47°, indicated by the blue bar) and Ni(2 2 0) (2θ = 14.681°, indicated by the red bar) during the annealing temperature range, two features are noticeable. One is that the peak, as a whole, shifts toward a higher angle with increasing temperature. We rationalized this phenomenon as reflecting the progress in IrNi solid solution alloying; Ni atoms diffuse into the Ir clusters, yielding a more homogeneous mixture of IrNi solid solution alloy. The other is the development of asymmetry in the peak; a ramp on the right-hand side of the peak begins to grow with an increase in temperature, particularly above 456 °C. This is likely to result from the enrichment of Ni in the IrNi solid-solution alloy cores and the segregation of Ir toward the core surfaces, induced by elevating temperatures.

When the temperature reached 600 °C in the quartz reactor, we maintained it constant for 2 h. We note that the peak position did not change, but its width decreased during these 2 h (Supporting Information, Figure S6). This finding demonstrates that the core−shell structure basically does not change, while the particles keep growing at 600 °C. After 2 h annealing at 600 °C, the particle size was 4.7 nm, i.e. identical to that examined by the XRD measurement with Cu Kα (Figure 1). As shown in the phase diagram (Figure S8),[24] the IrNi bulk system with 0.36 at % Ni forms a solid solution alloy below a temperature of 2000 °C. We consider that the segregation process (the enrichment of Ir atoms) occurs only at the surfaces (in the top two layers) above 450 °C, whereas the cores behave like the bulk; thus, the core−shell structure is kept at 600 °C.

The Rietveld refinement analyses were used to follow the changes in the cell dimensions and particle size with annealing temperature (Figure 7). We found that up to 220 °C the cell dimension of IrNi sample is approximately constant at 3.775 Å. This value is smaller than that of pure Ir metal (3.839 Å), but much larger than that of Ni metal (3.524 Å), pointing to the formation of Ir-rich phases in the nanoparticles. We designated the temperature region up to 220 °C as Regime I. Figure 7 also illustrates a schematic of the IrNi nanoparticle containing Ir-rich phases in this Regime. (Hexagonal-shaped particles are depicted just as an example.) Above 220 °C, the cell dimension starts to decline considerably with rising temperatures. We termed the region between 220 and 450 °C as Regime II. This cell contraction likely reflects further alloying of Ni with the Ir-rich clusters, generating in a more homogeneous IrNi alloy nanoparticle. From the Rietveld refinement we also estimated the particle size, which we present as a function of temperature. The particle size remains approximately constant (∼2.2 nm) up to 450 °C; thereafter, the particles start to grow up to 600 °C. We designated the region between 450 and 600 °C as Regime III. It is considered that the neighboring nanoparticles may migrate and coalesce on carbon-supports above 450 °C. Intriguingly, this onset temperature is almost coincident with that of the asymmetry in peak shape (Figure 6b) that is caused by the segregation of Ir atoms on the nanoparticle surfaces. Likely, long-range atomic diffusion occurs above 450 °C, and therefore, induces the segregation of Ir to the

particle surfaces as well as the growth of the particles, while below 450 °C atomic diffusion is confined to short-range order, presumably by the place-exchange mechanism. The formation of Ir shell on IrNi alloy core in Regime III is also illustrated schematically in Figure 7. As our EXAFS analysis revealed, the nanoparticles will eventually comprise the two layers of Ir on the IrNi alloy cores by thermal annealing at 600 °C.

It has been reported that the phenomenon of surface segregation is primarily determined by the surface energy and atomic size of alloy constituents.[15] Metal atoms having larger radii and lower surface energies usually tend to segregate to the surface. The experimental surface energies for Ir and Ni are 3.000 J m^{-2} and 2.450 J m^{-2},[49] and the metallic radii for Ir and Ni are 1.36 Å and 1.24 Å,[50] respectively. The Ir segregation for the present IrNi system can be predicted from the difference in radii but cannot be explained in terms of surface energies. It is known that Pt atoms tend to segregate to the surfaces of Pt−Ni system;[12] the radius of

Pt (1.39 Å) is much larger than that of Ni, while the surface energy of Pt (2.475 J m^{-2}) is almost comparable to that of Ni. This implies that the difference in atomic size is an important factor for the PtNi system; the segregation of Pt atoms to the surface alleviates strain in the alloy significantly, resulting in a decrease in the total energy.[15] A similar rationale may be applied to the Ir segregation for the IrNi system. On the other hand, Ruban et al. reported surface segregation energies for several transition-metal alloys to predict the surface segregation phenomena, based on density function calculations.[13] According to their calculations however, Ir atoms in a Ni bulk show a small but positive surface segregation energy, which corresponds that Ir atoms prefers to remain in the Ni bulk. This is in conflict with the experimental results identified by the present study; the discrepancy could be caused by the fact that the calculated surface segregation energy is in general proportional to the difference of the surface energies of the alloy components.[14] Refined theoretical approaches that can support the experimental observations are highly desired.

3.3. Catalytic Activity for Hydrogen Oxidation.
Figure 8a shows polarization curves of H$_2$ oxidation on the IrNi core−shell nanoparticles in a H$_2$-saturated 0.1 M HClO$_4$ solution at different rotation speeds. The currents exhibit rapid rises from zero to diffusion-limited plateaus within less than 100 mV. The behavior appears very similar to that observed for platinum that is known to be the best electrocatalyst for H$_2$ oxidation. The polarization curves of H$_2$ oxidation from a commercial Pt/C catalyst are shown in Supporting Information, Figure S7a together with those from a commercial Ir/C catalyst. Iridium shows relatively delayed responses for H$_2$ oxidation compared with Pt and the activity starts slightly to decline after attaining the maximum values. On the basis of the oxidation behavior and structural properties, it appears that Ni atoms in the IrNi cores improve the activity of H$_2$ oxidation on Ir surfaces. This is predominantly though the geometrical effect, i.e. contraction in Ir−Ir bond. The Ni-core-induced Ir shell contraction makes the surface less reactive for H$_2$O oxidation and IrOH formation (Figure S7c). The resulting more metallic Ir surface becomes more active for H$_2$ oxidation than the IrOH covered surface, as observed in Figure 8a. Figure 8b shows the mass activities (the kinetic currents divided by the masses) in H$_2$ oxidation from the IrNi nanoparticles and from commercial Pt/C and Ir/C catalysts at a potential of 0.05 V. The
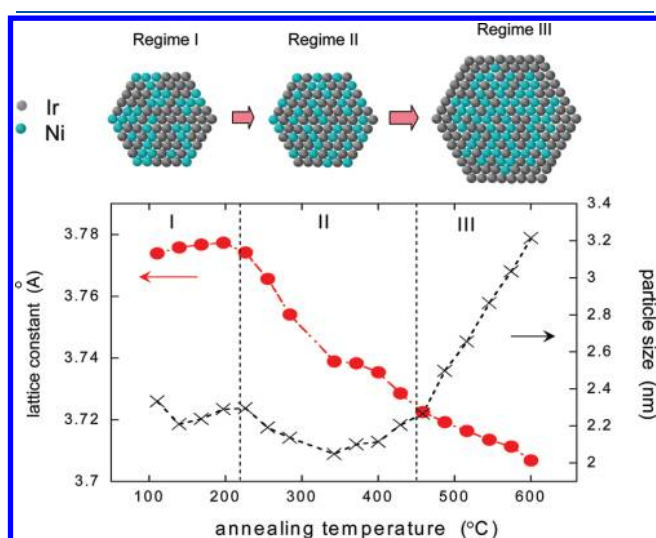

Figure 7. Rietveld refinement analyses showing changes in cell dimension and particle size of the IrNi nanoparticles as a function of annealing temperatures. Also shown is a schematic of changes in atomic structure of IrNi nanoparticles with increasing temperatures.
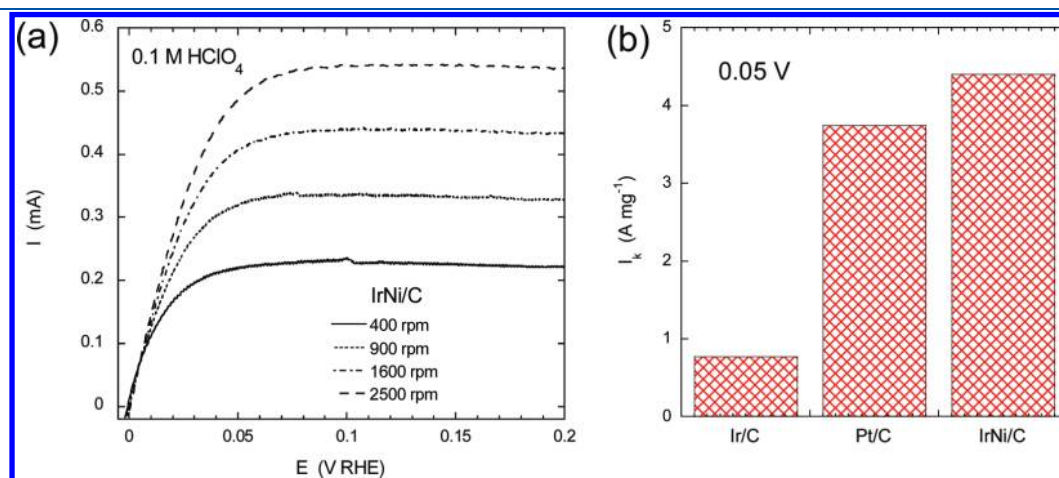

Figure 8. (a) Polarization curves for H$_2$ oxidation on IrNi core−shell nanoparticles in H$_2$-saturated 0.1 M HClO$_4$ (sweep rate: 10 mV s^{-1}) and (b) mass activity of H$_2$ oxidation from commercial Ir/C and Pt/C catalysts and the IrNi core−shell nanoparticles at a potential of 0.05 V. Metal loadings: 10.6 μg cm^{-2} (9.1 nmol) Ir for Ir/C, 7.6 μg cm^{-2} (6.4 nmol) Pt for Pt/C, 3.4 μg cm^{-2} (2.9 nmol) Ir and 0.58 μg cm^{-2} (1.6 nmol) Ni for IrNi/C.

kinetic currents were obtained from a Kouteky—Levich plot[39] shown in Supporting Information, Figure S7b. We calculated particle sizes from the XRD patterns and electrochemical surface areas by integrating the charges associated with the hydrogen desorption peaks in cyclic voltammograms (Figure S7c) and then determined the metal loadings of the catalysts using the ratio of surface to total atoms of nanoparticles as a function of particle size.[29] The mass activity of the IrNi core—shell nanoparticles (4.4 mA μg_{Ir+Ni}^{-1}) is ~6 times higher than that of the Ir/C catalysts (0.77 mA μg_{Ir}^{-1}); more interestingly it is even slightly higher than that of Pt/C catalyst (3.7 mA μg_{Pt}^{-1}), indicating that the IrNi nanoparticle catalyst is a promising candidate as non-Pt anode catalyst for H_2 oxidation.

4. CONCLUSIONS

We showed a simple method of synthesizing carbon-supported IrNi core—shell structured nanoparticles by chemical reduction, followed by thermal annealing in H_2. We detailed the structure of the Ir shell on the IrNi alloy using XRD, STEM—EELS, and in situ XAS. The EXAFS analysis is consistent with the model wherein the IrNi nanoparticles are composed of two-layer Ir shells and IrNi alloy cores. In situ XAS showed that the Ir shells completely protect the Ni atoms comprising the cores from oxidation or dissolution in an acid solution under elevated potentials. Time-resolved synchrotron XRD measurements combined with Rietveld refinement analyses demonstrated the process of reaching a homogeneous mixture of Ir and Ni atoms during thermal annealing above 220 °C, and the onset of Ir segregation on the IrNi core surfaces above 450 °C. Iridium is known as one of the most stable elements against corrosion;[34] thus, a shell comprising two Ir layers can protect non-noble metals such as Ni in cores, as this study clearly revealed (Figure 4b and Figure S7c). This new class of core—shell nanoparticles affords various possibilities for practical applications, such as electrocatalysts for fuel cells; one highly promising application is an anode electrocatalyst for hydrogen oxidation reaction as shown in the present study.

■ ASSOCIATED CONTENT

ⓢ Supporting Information. Additional STEM—EELS data, in situ time-resolved XRD, a low-resolution STEM image, in situ XAS, and structural parameters by the EXAFS analysis. This material is available free of charge via the Internet at http://pubs.acs.org.

■ AUTHOR INFORMATION

Corresponding Author

*E-mail: ksasaki@bnl.gov. Telephone: (+1-631) 3443446. Fax: (+1-631) 3445815.

■ ACKNOWLEDGMENT

■ REFERENCES

(1) Zhang, J.; Lima, F. H. B.; Shao, M. H.; Sasaki, K.; Wang, J. X.; Hanson, J; Adzic, R. R. *J. Phys. Chem. B* **2005**, *109*, 22701–22704.

(2) Shao, M; Sasaki, K; Marinkovic, N. S.; Zhang, L.; Adzic, R. R. *Electrochem. Commun.* **2007**, *9*, 2848–2853.

(3) Yan, J. M.; Zhang, X. B.; Akita, T.; Haruta, M.; Xu, Q. *J. Am. Chem. Soc.* **2010**, *132*, 5326–5327.

(4) Alayaglu, S.; Zavalij, P.; Eichhorn, B.; Wang, Q.; Frenkel, A. I.; Chupas, P. *ACS Nano* **2009**, *3*, 3127–3137.

(5) Lee, Y. W.; Kim, M.; Kim, Z. H.; Han, S. W. *J. Am. Chem. Soc.* **2009**, *131*, 17036–1737.

(6) Tao, F.; Grass, M. E.; Zhang, Y.; Butcher, D. R.; Renzas, J. R.; Liu, Z.; Chung, J. Y.; Mun, B. S.; Salmeron, M.; Somorjai, G. A. *Science* **2008**, *7*, 932–934.

(7) Alayaglu, S.; Nilekar, A. U.; Mavrikakis, M.; Eichhorn, B. *Nat. Mater.* **2008**, *7*, 333–338.

(8) Cui, Y.; Ren, B.; Yao, J. L.; Gu, R. A.; Tian, Z. Q. *J. Phys. Chem. B* **2006**, *110*, 4002–4006.

(9) Scott, R. W. J.; Wilson, O. M.; Oh, S. K.; Kenik, E. A.; Crooks, R. M. *J. Am. Chem. Soc.* **2004**, *126*, 15583–15591.

(10) Mallin, M. P.; Murphy, C. J. *Nano Lett.* **2002**, *2*, 1235–1237.

(11) Mani, P.; Srivastava, R.; Strasser, P. *J. Phys. Chem. C* **2008**, *112*, 2770–2778.

(12) Fowler, B; Lucas, C. A.; Omer, A; Wang, G; Stamenkovic, V. R.; Markovic, N. M. *Electrochim. Acta* **2008**, *53*, 6076–6080.

(13) Ruban, A. V.; Skriver, H. L.; Nørskov, J. K. *Phys. Rev. B* **1998**, *59*, 15990–16000.

(14) Christoffersen, E.; Liu, P.; Ruban, A.; Skriver, H. L.; Nøskov, J. K. *J. Catal.* **2001**, *199*, 23–131.

(15) Ma, Y.; Balbuena, P. B. *Surf. Sci.* **2008**, *602*, 107–113.

(16) Hammer, B.; Nørskov, J. K. *Adv. Catal.* **2000**, *45*, 71–129.

(17) Mavrikakis, M.; Hammer, B.; Nørskov, J. K. *Phys. Rev. Lett.* **1998**, *81*, 2819–2822.

(18) Naitabdi, A.; Ono, L. K.; Behafarid, F.; Cuenya, B. R. *J. Phys. Chem. C* **2009**, *113*, 1433–1446.

(19) Nashner, M. S.; Frenkel, A. I.; Somerville, D.; Hills, C. W.; Shapley, J. R.; Nuzzo, R. G. *J. Am. Chem. Soc.* **1998**, *120*, 8093–8101.

(20) Hodak, J. H.; Henglein, A.; Giersig, M.; Hartland, G. V. *J. Phys. Chem. B* **2000**, *104*, 11708–11718.

(21) Normile, P. S.; De Toro, J. A.; Andres, J. P.; Gonzalez, J. A.; Munoz, T.; Muniz, P.; Barbero, A. J.; Riveiro, J. M. *J. Appl. Phys.* **2006**, *100*, 064312–064314.

(22) Adzic, R. R.; Wang, J. X.; Ocko, B. M.; McBreen, J. In *Electrocatalysis*; Vielstich, W., Lamm, A. G., Gasteiger, H. A., Eds.; Handbook of Fuel Cells: Fundamentals, Technology and Applications, Vol. 2, John Wiley & Sons: Chichester, 2003; pp 279—301.

(23) Sasaki, K.; Adzic, R. R. *Synchrotron Radiat. News* **2009**, *22*, 17–21.

(24) http://www.asminternational.org/asmenterprise/apd.

(25) Pearson, W. B. *Handbook of Lattice Spacings and Structures of Metals and Alloys*; Pergamon Press: New York, 1967; Vol. 2, pp 592—705.

(26) Cullity, B. D.; Stock, S. R. *Elements of X-Ray Diffraction*, 3rd ed.; Prentice-Hall Inc.: New York2001; pp 167—171.

(27) Kinoshita, K. In *Modern Aspects of Electrochemistry*; Bockris, J. O'. M., Conway, B. E., White, R. E., Eds.; Plenum Press; New York, 1982; Vol. 14, pp 557—637.

(28) Benfield, R. E. *J. Chem. Soc. Faraday Trans.* **1992**, *88*, 1107–1110.

(29) McBreen, J.; Mukerjee, S. In *Interfacial Electrochemistry: Theory, Experiment, and Applications*; Wieckowski, A., Ed.; Marcel Dekker: New York, 1999; pp 895—914.

(30) This is defined as the energy of first derivative of the spectrum.

(31) Jiang, D. T.; Sham, T. K.; Norton, P. R. *Phys. Rev. B* **1994**, *49*, 3709–3712.

(32) Couves, J. W.; Meehan, P. *Physica B* **1995**, *208 and 209*, 665–667.

9901

dx.doi.org/10.1021/jp200746j |*J. Phys. Chem. C* 2011, 115, 9894–9902

(33) Sasaki, K.; Zhang, J.; Wang, J. X.; Uribe, F.; Adzic, R. R. *Res. Chem. Intermed.* **2006**, *32*, 543–559.

(34) Pourbaix, M. *Atlas of Electrochemical Equilibria in Aqueous Solutions*; Pergamon/CEBELCOR: Oxford, 1966; pp330−342, pp373−377.

(35) Frenkel, A. I. *Z. Kristallogr.* **2007**, *222*, 605–611.

(36) Glasner, D.; Frenkel, A. I. *AIP Conf. Proc.* **2007**, *882*, 746–748.

(37) Coordinates of polyhedral clusters are available from: http://www3.bnl.gov/frenkel/coords.html. For the program to calculate the properties of bimetallic nanoparticles please contact A. I. Frenkel (anatoly.frenkel@yu.edu).

(38) With an increase in temperature, the XRD peak positions shift to lower angles due to an increase in the thermal expansion of the lattice. Assuming that the thermal expansion with elevating temperature is linear, we corrected the peak positions in Figure 6 as well as the lattice constants in Figure 7.

(39) Levich, V. G. *Physicochemical Hydrodynamics*; Prentice-Hall: Englewood Cliffs, NJ, 1962.

(40) McBreen, J.; O'Grady, W. E.; Pandya, K. I.; Hoffman, R. W.; Sayers, D. E. *Langmuir* **1987**, *3*, 428–433.

(41) Sasaki, K.; Wang, J. X.; Naohara, H.; Marinkovic, N.; More, K.; Inada, H.; Adzic, R. R. *Electrochim. Acta* **2010**, *55*, 2645–2652.

(42) http://x18b.nsls.bnl.gov.

(43) Ravel, B.; Newville, M. *J. Synchrotron Radiat.* **2005**, *12*, 537.

(44) Rodriguez, J. A.; Hanson, J. C.; Wen, W.; Wang, X.; Brito, J. L.; Martinez-Arias, A.; Fernandez-Garcia, M. *Catal. Today* **2009**, *145*, 188–194.

(45) Barrio, L.; Estrella, M.; Zhou, G.; Wen, W.; Hanson, J. C.; Hungria, A. B.; Hornes, A.; Martinez-Arias, A.; Fernandez-Garcia, M.; Rodriguez, J. A. *J. Phys. Chem. C* **2010**, *114*, 12689–12697.

(46) Toby, B. H. *J. Appl. Crystallogr.* **2001**, *34*, 210–213.

(47) Larson, A. C.; von Dreele; R. B. *General Structure Analysis System (GSAS)*; Los Alamos National Laboratory: Los Alamos, NM, 1995; Report LAUR 86-748.

(48) Rietveld, H. M. *J. Appl. Crystallogr.* **1969**, *2*, 65–71.

(49) De Boer, F. R.; Boom, R.; Mattens, W. C. M.; Miedema, A. R.; Niessen, A. K. *Cohesion in Metals*; Amsterdam: North-Holland, 1998.

(50) Greenwood, N. N.; Earnshaw, A. *Chemistry of the Elements*, 2nd ed.; Butterworth-Heinemann: Oxford, 1997.